www.sciencemag.org/content/344/6191/1496/suppl/DC1

Supplementary Materials for

Observing liquid flow in nanotubes by 4D electron microscopy

Ulrich J. Lorenz and Ahmed H. Zewail*

*Corresponding author. E-mail: zewail@caltech.edu

Published 27 June 2014, *Science* **344**, 1496 (2014)
DOI: 10.1126/science.1253618

This PDF file includes:

Other supplementary material for this manuscript includes the following:

Movies S1 and S2

Materials and Methods

Lead filled ZnO nanotubes were synthesized as previously described (*17*). Briefly, a 1x1 mm piece of zinc foil was immersed into a 1 mM aqueous solution of $Pb(NO_3)_2$ after its surface had been thoroughly scratched with a razor blade. After several minutes when a dense forest of whiskers had formed on its surface, the zinc foil was carefully removed, washed by dipping into deionized water, and dropped into 0.5 ml methanol. The nanotubes were detached from the surface by gentle shaking. Typically, 5 µl of the resulting suspension were then deposited onto a TEM grid (1-6 monolayer thick graphite film on 2000 mesh copper, Graphene Supermarket), and the solvent was allowed to evaporate.

Time-resolved single-shot experiments were carried out with the UEM-1 instrument (*15*). Unless otherwise noted, the sample was held at 363 K. Dynamics were initiated with a 532 nm pulsed picosecond laser that was focused onto the specimen (16 ps FWHM, 20 µm FWHM spot size, and 150 nJ pulse energy, unless otherwise noted). The structure was then imaged at a given time delay with a probe electron pulse generated by a 266 nm nanosecond laser (10 ns FWHM) that was synchronized to the pump laser with a digital delay generator. In order to eliminate the 20 ns jitter between the pump and probe pulse, both laser pulses were monitored with fast photodiodes, and their precise delay was determined for every experiment.

A bandpass filter was applied to the single-shot images and any images recorded with a pulsed electron beam. Occasionally, a small shift between the images recorded before and after the pump laser pulse was observed, which may be due to some deformation of the substrate. The images are shown without correction for this shift. In general, we have limited our discussion to displacements much larger than typical image drift or to observations that could not possibly be explained by a movement of the entire sample. We also note that the tubes are attached to the substrate and therefore do not undergo any large-amplitude mechanical movement induced by the laser pulse, so that one could mistake such a motion for an expansion of the lead column. Moreover, when irregularities of the tube walls are recognizable in the single-shot images, it is

evident that the liquid column moves past these points, which could not be explained by a movement of the entire tube.

In order to measure the expansion of a laser heated lead column as a function of time (see Fig. 4 of the main text), we determine the center of the meniscus in the images recorded before and shortly after the laser pulse. The displacement of the center is then projected onto the tube axis, and the norm is taken to obtain the expansion. The center of the meniscus is first guessed for every image. Subsequently, an intensity profile is taken at this point orthogonal to the tube axis. A fit with a top hat shaped function serves to obtain the exact location of the tube axis, and the guess for the center of the meniscus is updated accordingly. Finally, an intensity profile is calculated at this new location, this time parallel to the tube axis. A fit with an error function then serves to update the position of the meniscus parallel to the axis. The error bars shown in Fig. 4 of the main text are derived from the standard errors of the fit. Occasionally, bad fits result in errors larger than 20 nm, and the corresponding data points are discarded. It should be noted that this procedure gives the displacement of the meniscus averaged over its width.

Supplementary Text

Estimation of the temperature-jump and cooling rate

The transient temperature of a sample can be conveniently determined from a time-resolved diffraction experiment by means of the Debye-Waller effect, which predicts an exponential decrease of the scattered intensity with temperature (*34*). However, non-Debye-Waller behavior is observed if the sample undergoes a phase transition. We therefore estimate the transient temperature of the lead filled ZnO nanotubes from an experiment conducted at lower laser fluences and extrapolate to the fluence used in the single-shot experiments. In order to obtain a diffraction pattern with a sufficient signal-to-noise ratio, it is necessary to average the results of many individual experiments. However, the delicate nanotubes would not be able to withstand exposure to millions of laser shots at a high fluence. Moreover, such a stroboscopic measurement requires that the sample does not undergo irreversible changes, which would

obscure the dynamics. This is not the case at high laser fluence, where we observe that the ordered domains of the lead core become mobile and randomly change their orientation. It is found that such irreversible processes can only be sufficiently suppressed when the pulse energy is limited to 15 nJ (one tenth of the energy used for the single-shot experiments).

Figure S1A shows a partially filled nanotube with an average outer diameter of 85 nm of the filled sections. An aperture was inserted to record the selected-area diffraction (SAD) pattern of fig. S1B. It shows reflections of the graphite substrate as well as the circled groups of diffractions spots, which arise from domains of the lead core that fulfill the Bragg condition. The diffraction intensity was determined by radially averaging the corresponding sections of the diffraction pattern and fitting the obtained intensity profiles in the vicinity of the peaks with the sum of a Lorentzian and a quadratic background function.

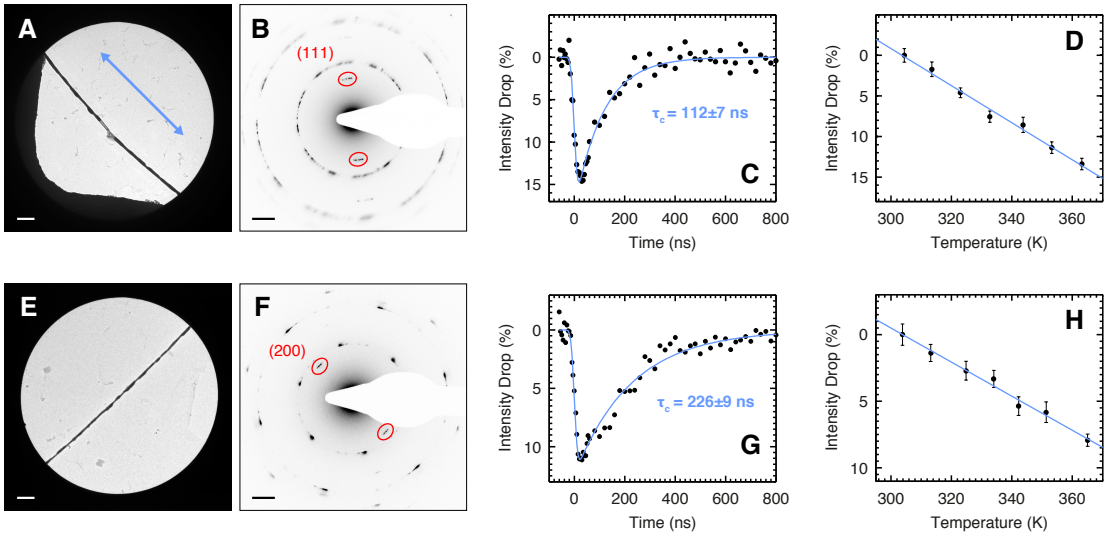

Fig. S1. Estimation of the temperature-jump and cooling rate for two different nanotubes. **(A, E)** Micrographs of the nanotubes; the laser polarization is indicated with a double headed arrow. (Scale bars, 500 nm.) **(B, F)** The corresponding selected-area diffraction patterns show groups of reflections (circled in red) arising from domains of the lead core that fulfill the Bragg condition. (Scale bars, 2 nm^{-1}.) **(C, G)** Integrated intensity of these groups of diffraction peaks as a function of the time delay between the laser pump and electron probe pulse. The blue curve represents a

fit with an exponential function, broadened to account for the temporal jitter and the finite width of the probe pulse. **(D, H)** Plot of the diffraction intensity as a function of the sample temperature in the absence of the pump laser. Error bars indicate ±1 SEM of 20 measurements for every data point.

Figure S1C shows the summed intensity of both groups of reflections as a function of delay between the laser pump and electron probe pulses. Unlike in the single-shot experiments discussed in the main text, which were carried out at 363 K, the sample was held at room temperature. We find that the observed cooling dynamics, which represent an average over the length of the tube, can be well described by a single exponential with a time constant of 112 ns (blue line). This result is obtained by forward convolution taking into account the jitter between the pump and probe of 20 ns and the Gaussian profile of the electron pulse with 10 ns FWHM. We also measured the diffraction intensity as a function of the sample temperature (in the absence of laser irradiation), which is shown in fig. S1D. A linear fit of the logarithm of the diffraction intensity provides a calibration for the transient data, which allows us to determine that the nanotube undergoes an initial temperature-jump of 81 K.

By fitting the logarithm of the diffraction intensity with a straight line, Debye-Waller behavior is implied. However, partial melting of the sample (non-Debye-Waller behavior) or movement of the diffracting domains may also contribute to the observed intensity changes. The linear relationship may nevertheless serve to estimate the transient temperature profile, assuming that any processes leading to a change in diffraction intensity are fast compared with the cooling rate, *i.e.* the lead core is always in a state of quasi-equilibrium.

Figures S1E-G show data for a second nanotube with an average outer diameter of 61 nm, for which we determine a temperature-jump of 106 K. Cooling occurs with a time constant of 226 ns.

The first tube dissipates heat faster, likely because it is located closer to the copper bars of the TEM grid (fig. S1A, left and bottom), which act as a heat sink.

For nanoparticles, thermal equilibriation occurs on a timescale of 100 ps (*35*), much faster than heat dissipation. Thus the lead column and ZnO shell reach thermal equilibrium promptly after the laser pulse. For a nanotube initially at temperature T_0 and reaching T_1 after the temperature-jump, the energy ΔQ absorbed by a small section of length Δx is then given by,

$$\frac{\Delta Q}{\Delta x} = \pi r^2 \rho^{\mathrm{Pb}} \int_{T_0}^{T_1} C_p^{\mathrm{Pb(s)}} \mathrm{d}T \; + \; \pi(w^2 + 2rw)\rho^{\mathrm{ZnO}} \int_{T_0}^{T_1} C_p^{\mathrm{ZnO}} \mathrm{d}T \qquad (1)$$

where r is the radius of the lead core and w the thickness of the tube wall; $C_p^{\mathrm{Pb(s)}}$ and C_p^{ZnO} are the specific heat capacities of solid lead (*36*) and ZnO (*37*), respectively; and ρ^{Pb} = 11343 kg/m^3 and ρ^{ZnO} = 5606 kg/m^3 are their densities. The average outer diameters $2(r + w)$ of the nanotubes in fig. S1A and E (85 and 61 nm, respectively) were deduced from intensity profiles taken orthogonal to the tube axis along the full length of the filled sections. The mean width of the tube was then determined from fits with top hat profiles. For the thickness of the ZnO shell, we deduce w = 10 nm for both tubes. Using Equation (1), we find that the first tube (fig. S1A) absorbs about 40 % more energy per unit length than its counterpart of fig. S1E, which is consistent with its larger geometric cross section. It is oriented parallel to the laser polarization, which is indicated with a double headed arrow in fig. S1A. However, most nanotubes that we investigated happened to be oriented parallel to the second tube (fig. S1E), *i.e.* nearly orthogonal to the laser polarization. We therefore used the data gathered for the second tube (fig. S1E-H) for the temperature-jump calculation. We note that estimates obtained with the first data set are qualitatively similar, and the differences are insubstantial for any of the conclusions drawn in the main text.

We estimate the temperature of a given nanotube in a single-shot experiment by extrapolating to a high fluence while taking the geometry of the tube into account. In our calculation, it is assumed that the energy absorbed per unit length $\Delta Q/\Delta x$ is proportional to the laser fluence and that we do

not saturate the optical transition. This should be a good approximation, given that electron-electron scattering occurs on the fs time scale, much faster than the duration of our pump laser pulse of 16 ps FWHM (*38*). Indeed, it was found that the temperature of a laser heated Pb(111) surface increases linearly with the fluence until melting sets in, albeit at a longer laser pulse duration of 180 ps (*34*). The same observation was made for gold nanoparticles, this time with 150 fs laser pulses (*35*). The absorption cross section is taken to be proportional to the geometric cross section of the lead core, *i.e.* to its radius *r*. Numerical simulations of the absorption cross section of an infinitely long lead nanowire coated with a ZnO shell suggest that this is a reasonable approximation for tube radii close to the one determined in fig. S1E and when the incident laser is polarized orthogonal to the tube axis.

For a nanotube heated above the melting point of lead, the energy absorbed per unit length $\Delta Q/\Delta x$ is thus given by,

$$\frac{\Delta Q}{\Delta x} = \pi r^2 \rho^{\mathrm{Pb}} \left[\int_{T_0}^{T_m} C_p^{\mathrm{Pb(s)}} \mathrm{d}T \; + \; \Delta \mathrm{H_f} \; + \int_{T_m}^{T_1} C_p^{\mathrm{Pb(l)}} \mathrm{d}T \right] + \pi (w^2 + 2rw) \rho^{\mathrm{ZnO}} \int_{T_0}^{T_1} C_p^{\mathrm{ZnO}} \mathrm{d}T \qquad (2)$$

where T_m = 600.64 K is the melting point of lead (*18*), ΔH_f = 23.1 kJ/kg its specific heat of fusion (*39*), and $C_p^{\mathrm{Pb(l)}}$ the specific heat capacity of liquid lead (*18*). By calculating $\Delta Q/\Delta x$ using the assumptions discussed above and then solving Equation (2) for T_1, we obtained the temperature of the nanotube after the laser pulse.

Model of the expansion dynamics of a lead column inside a nanotube

We model the laser driven expansion and subsequent contraction of liquid lead inside a nanotube in analogy with the derivation of Washburn's law, which successfully describes the filling dynamics of a vertical capillary brought into contact with a liquid (*22*). The vertical liquid column of mass *m*, moving with velocity *v*, is drawn into the capillary by the capillary force *F*, while the weight of the column *W* and the viscous friction force F_η oppose its progression.

$$\frac{d(mv)}{dt} = F - F_\eta - W \tag{1}$$

The friction force F_η is derived from Poiseuille's law for laminar flow of an incompressible Newtonian fluid through a pipe with circular cross section

$$F_\eta = 8\pi\eta v z, \tag{2}$$

where η is the dynamic viscosity and *z* the length of the column.

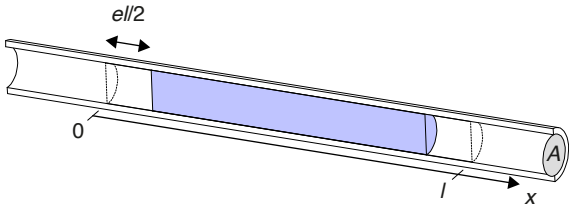

Fig. S2. Schematic drawing of a liquid filled nanotube and definition of relevant parameters.

In a horizontal nanotube (fig. S2), we can neglect the weight *W*. Moreover, we can neglect the capillary force *F*, which is small and remains constant. However, we have to choose a continuum treatment to describe the expansion of the liquid. The forces acting on a short section of the column with length *Δx are*

$$A\Delta x\rho\ddot{u} = AE\frac{\partial^2 u}{\partial x^2}\Delta x - \dot{u}f\Delta x, \tag{3}$$

where *u* is the displacement field, *A* the cross section of the column, ρ the density of lead, *f* the friction coefficient, and *E* the resistance of the liquid column to compression in the axial direction. For a rigid tube, *E* can be identified with the bulk modulus *K*

$$E = K = -V\frac{dp}{dV}, \tag{4}$$

where *V* is the volume and *p* the pressure of the column. If the tube expands at high temperature and high internal pressure, *E* is effectively reduced. We neglect the volume viscosity of lead since its effect on the dynamics is small as we verified by solving Equation 3 numerically while including the volume viscosity. As discussed in more detail below, we also neglect the energy cost of

displacing and deforming the meniscus as well as other forms of energy dissipation which reduce the speed of the expanding column.

Simplifying Equation 3 gives

$$\ddot{u} = \frac{E}{\rho}\frac{\partial^2 u}{\partial x^2} - \frac{f}{A\rho}\dot{u} \quad . \tag{5}$$

The initial displacement is

$$u(x, t = 0) = \frac{el}{2} - ex \quad , \tag{6}$$

where *e* is the compression per unit length of the column with respect to *l*, its equilibrium length at the temperature it reaches immediately after the laser pulse. Moreover, the system is initially at rest

$$\dot{u}(x, t = 0) = 0 \quad . \tag{7}$$

We observe that the lead column returns to its initial temperature on a time scale of about 300 ns (fig. S1). It is nevertheless instructive to solve Equations 5-7 assuming that no cooling takes place after the laser pulse, so that the equilibrium length *l* does not change with time. The solution provides a good approximation for the initial expansion of the column, where the temperature can be assumed to be constant. In order to model the dynamics at later times, we then to resort to numerical simulations.

It should be noted that under the assumption of constant temperature, Equations 5-7 also describe the damped oscillations of an initially compressed free prismatic bar, where *E* then represents Young's modulus of its material (*40*). The solution is found by setting

$$u(x, t) = \sum_n q_n \cos\frac{n\pi x}{l} \quad , \tag{8}$$

where q_n are time dependent coefficients. One obtains a set of differential equations for the coefficients

$$\ddot{q}_n + \frac{f}{A\rho}\dot{q}_n + \frac{E\pi^2 n^2}{\rho l^2} q_n = 0 \tag{9}$$

with the characteristic equations

$$\lambda_n = -\frac{f}{2A\rho} \pm \sqrt{\frac{f^2}{4A^2\rho^2} - \frac{E\pi^2 n^2}{\rho l^2}} \quad . \tag{10}$$

For small damping, the roots λ_n are complex, so that we can write

$$\lambda_n = -\frac{f}{2A\rho} \pm i\omega'_n \quad . \tag{11}$$

In the undamped case ($f = 0$), the roots λ_n are

$$\lambda_n = \pm i\omega_n = \pm i\sqrt{\frac{E}{\rho}}\frac{\pi n}{l} \quad . \tag{12}$$

This yields the general solution for q_n

$$q_n = e^{-\frac{f}{2A\rho}t} \cdot (A_n \cos(\omega'_n t) + B_n \sin(\omega'_n t)), \tag{13}$$

where the coefficients A_n and B_n can be determined by using the initial conditions (Equations 6 and 7). For small f, $B_n \approx 0$, and one obtains

$$u = e^{-\frac{f}{2A\rho}t} \cdot \frac{4el}{\pi^2} \sum_{n=1,3,5,\ldots} \frac{1}{n^2} \cos(\omega'_n t) \cos(\frac{n\pi x}{l}) \quad . \tag{14}$$

For the displacement of the meniscus ($x = l$), we obtain

$$u_{x=l} = -e^{-\frac{f}{2A\rho}t} \cdot \frac{4el}{\pi^2} \sum_{n=1,3,5,\ldots} \frac{1}{n^2} \cos(\omega'_n t) \quad , \tag{15}$$

which for small damping ($\omega'_n \approx \omega_n$) becomes

$$u_{x=l} = -e^{-\frac{f}{2A\rho}t} \cdot \frac{4el}{\pi^2} \sum_{n=1,3,5,\ldots} \frac{1}{n^2} \cos(\omega_n t) \quad . \tag{15b}$$

Equation 15b is a product of a triangle wave $f_{triangle}$

$$f_{\text{triangle}} = \frac{el}{2}\left[\frac{8}{\pi^2} \sum_{n=1,3,5,\ldots} \frac{1}{n^2} \cos(n\omega_1 t)\right], \tag{16}$$

which describes the motion in the absence of friction ($f = 0$) with an exponential function that describes frictional damping. The triangle wave has an amplitude of $el/2$ and a period τ

$$\tau = \frac{2\pi}{\omega_1} = 2l \cdot \sqrt{\frac{\rho}{E}} \quad . \tag{17}$$

The meniscus therefore initially moves with a speed v_0

$$v_0 = e \cdot \sqrt{\frac{E}{\rho}}, \tag{18}$$

and we can express its displacement from its initial position $\Delta u_{x=l}$ as

$$\Delta u_{x=l} = \frac{el}{2} + e^{-\frac{f}{2A\rho}t} \cdot \left(-\frac{el}{2} + v_0 t \right). \tag{19}$$

Equation 19 expresses an intuitive result. Friction slows the initial expansion so that $\Delta u_{x=l}$ deviates from linearity. Our experimental data (Fig. 4 of the main text) suggest that frictional damping must be small since the expansion curve does not deviate strongly form a straight line. We estimate the friction coefficient *f* by fitting the expansion curve with the expression

$$\Delta u_{x=l} = \frac{el}{2} + e^{-\frac{f}{2A\rho}(t-t_0)} \cdot \left(-\frac{el}{2} + v_0 (t - t_0) \right), \tag{20}$$

where the parameter t_0 allows for a delayed onset of the expansion; the cross section of the column *A* and density ρ are known, the velocity v_0 is obtained from a linear fit of the expansion curve, and *el*/2 is estimated to be the maximum displacement of the meniscus. We verified this procedure by fitting simulated expansion curves with Equation (20). The fit reproduces the friction coefficient of the simulation well and rather overestimates it in the case of very small fricition. We find that the fit is not very sensitive to different values of *el*/2, which allows us to simply estimate *el*/2 from the maximum expansion. Estimates of the friction coefficient in Fig. 4 of the main text using different values of *el*/2 fall within the indicated range. We note that in the regime of small *f*, Equation 20 becomes

$$\Delta u_{x=l} \approx \left(\frac{elf}{4A\rho} + v_0 \right) \cdot (t - t_0) - \frac{f}{2A\rho} v_0 \cdot (t - t_0)^2. \tag{21}$$

In the following, we compare the analytical expressions derived above as well as the results of numerical simulations with the experimental data. Figure S3A shows the measured expansion of a lead column inside a nanotube of 55 nm inner diameter as a function of the time after the heating pulse. As described in the main text (see the discussion of Fig. 4), we estimate the friction

coefficient from a fit (Equation 20, blue line) of the initial expansion (data points in blue). To validate this procedure, we show that our model can reproduce the observed dynamics.

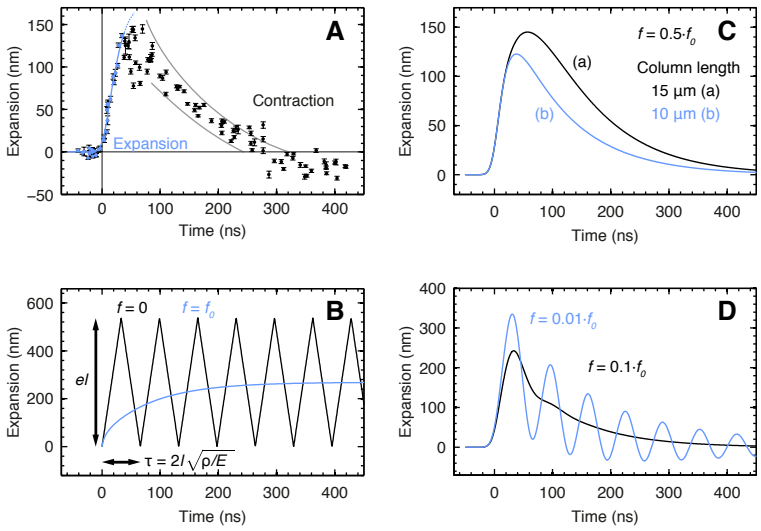

Fig. S3. Simulation of the expansion dynamics of a liquid lead column inside a nanotube following impulsive laser heating. **(A)** Experimental data for a nanotube of 55 nm inner diameter. The friction coefficient f is estimated from a fit (blue line) of the initial expansion (blue dots). The gray lines provide a guide for the eye. Error bars indicate the standard error of the fit used to extract the displacement of the meniscus. **(B)** Simulation using the analytical solution of Equation 9 assuming a fixed temperature after the laser pulse for $f = 0$ (black) and $f = f_0 = 8\pi\eta$ (blue); the column length was chosen to be $l = 15$ µm. **(C)** Numerical simulations for column lengths $l = 15$ µm (black) and $l = 10$ µm (blue); $f = 0.5 \cdot f_0$. The equilibrium column length is assumed to decrease exponentially after the laser pulse. The curves are convoluted with a Gaussian function of 10 ns FWHM to account for the finite electron pulse duration. **(D)** Numerical simulations for $f = 0.1 \cdot f_0$ (black) and $f = 0.01 \cdot f_0$ (blue); $l = 15$ µm.

In the following, the diameter of the lead column is 55 nm, as determined from the micrograph of fig. S6. The length l of the column cannot be measured since the nanotube extends beyond the transparent region of the specimen support. We assume a typical value of $l = 15$ µm and assess the effect of a variation of the column length. Using the procedure outlined above, the

temperature of the tube immediately after the laser pulse is estimated to be 1700 K, well above the melting point of lead T_m = 600.64 K (*18*). The bulk modulus of lead at this temperature K(1700 K) = 23.5 GP (*33*) can serve as an upper limit of the resistance of the liquid column to compression E. The upper limit for the initial compression per unit length is $e = 1-\rho_l/\rho_s$, where ρ_l = 9309 kg/m^3 is the density of liquid lead at 1700 K (*33*), and ρ_S = 11343 kg/m^3 the density of solid lead. The values of both E and e are effectively reduced if the tube expands under pressure or if the lead column does not fully return to its low-temperature equilibrium length upon cooling. Both E and e determine the speed of the initial expansion v_0 via Equation 18, which can also be obtained from energy conservation by equating the elastic energy stored in a short section of the column of length Δx to its kinetic energy after it has expanded,

$$\frac{1}{2}e^2 EA\Delta x = \frac{1}{2}A\Delta x\rho v_0^2 \quad . \tag{22}$$

While our model accounts for viscous friction, the expanding column may also dissipate energy for displacing and deforming the meniscus and possibly for detaching from the tube wall, which may be associated with a significant energy cost if an oxide skin covers the liquid column (*27*). All these additional sources of energy dissipation, when added to Equation 22, reduce the amount of energy available for accelerating the column and thereby decrease v_0, leading to lower effective values of E and e. We note that in Equation 20, which we use to extract the friction coefficient from our experimental data, v_0 becomes a mere fit parameter incorporating both e and E. When we set $E = 0.1\cdot K$(1700 K) and $e = 0.2\cdot(1 - \rho_l/\rho_s)$, the simulated speed of the initial expansion v_0 closely matches the experimental data. With these parameters, our simulations also predict the maximum expansion reasonably well, which among other factors depends on e. For the density of lead, we take $\rho = \rho_S$.

Figure S3B displays expansion dynamics simulated using the analytical solution of Equation 9 with a fixed temperature after the laser pulse. Without damping (f = 0, black curve), elastic oscillations occur, which are described by a triangle wave with amplitude $el/2$ and period $\tau = 2l\cdot(\rho/E)^{1/2}$ (Equation 17). If we set $f = f_0 = 8\pi\eta$, where $\eta = 8.53\cdot10^{-4}$ Pa·s is the dynamic viscosity of lead at 1700 K (*33*), we obtain the overdamped blue curve.

Solving Equation 9 numerically allows us to simulate the complete dynamics of expansion and contraction. We neglect that the lead core undergoes a phase transition upon cooling and assume that the equilibrium length of the column decreases exponentially from l to an asymptotic value of (l-el) with a time constant of 100 ns (a typical 1/e time for cooling of a nanotube in close proximity to a copper bar of the TEM grid, see above). The friction coefficient f is taken to be constant. When $f = 0.5 \cdot f_0$, we obtain the black curve in fig. S3C, which basically reproduces the experimental data. When the equilibrium length is decreased to 10 µm, the blue curve is obtained. The velocity of the meniscus during the initial expansion v_0 is identical, as predicted by Equation 18, which states that v_0 is independent of the column length l. Moreover, the maximum expansion decreases only by about 20%. The small changes of the column length that sometimes occur in the course of an experiment therefore only lead to a minor distortion of the measured dynamics. Most importantly, they will not affect the initial expansion, which we use to estimate the friction coefficient f.

In fig. S3D, the friction coefficient is further reduced to $f = 0.1 \cdot f_0$ (black curve) and $f = 0.01 \cdot f_0$ (blue curve), which is close to the estimate obtained from the experimental data. At such low damping, oscillations of the meniscus are predicted to occur. It is possible that these oscillations contribute to the increased scatter of the data points that we observe once the lead column has reached its maximum expansion. However, several effects that our model neglects might suppress such elastic oscillations. For example, we assume that the liquid column always fills the entire cross section of the tube. This might not be true if the column is stretched beyond its equilibrium length and give rise to an additional process in which the kinetic energy is dissipated. It is also conceivable that static friction might set in once the velocity of the advancing column has dropped below a critical value, thus altering the observed dynamics. Finally, if the slip length should indeed depend nonlinearly on the shear rate, as discussed in the main text, the friction coefficient f would be higher during the slow contraction of the column, which would lead to fast damping of the oscillations.

The important point here is that the friction coefficient can be measured experimentally, and in this case from the measured (in the image) expansion as a function of time, we can ascertain that this coefficient is small, being at most 10 % of the bulk value of liquid lead (see the main text).

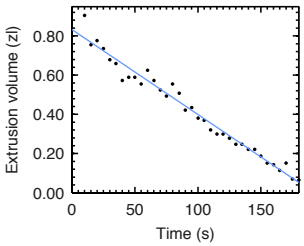

Fig. S4. Volume of the extrusion in Fig. 1B-F of the main text and Movie S2 as a function of time. The volume is estimated from the particle diameter assuming spherical shape. A linear fit (blue line) yields an average flow rate of about 4 yoctolitres per second.

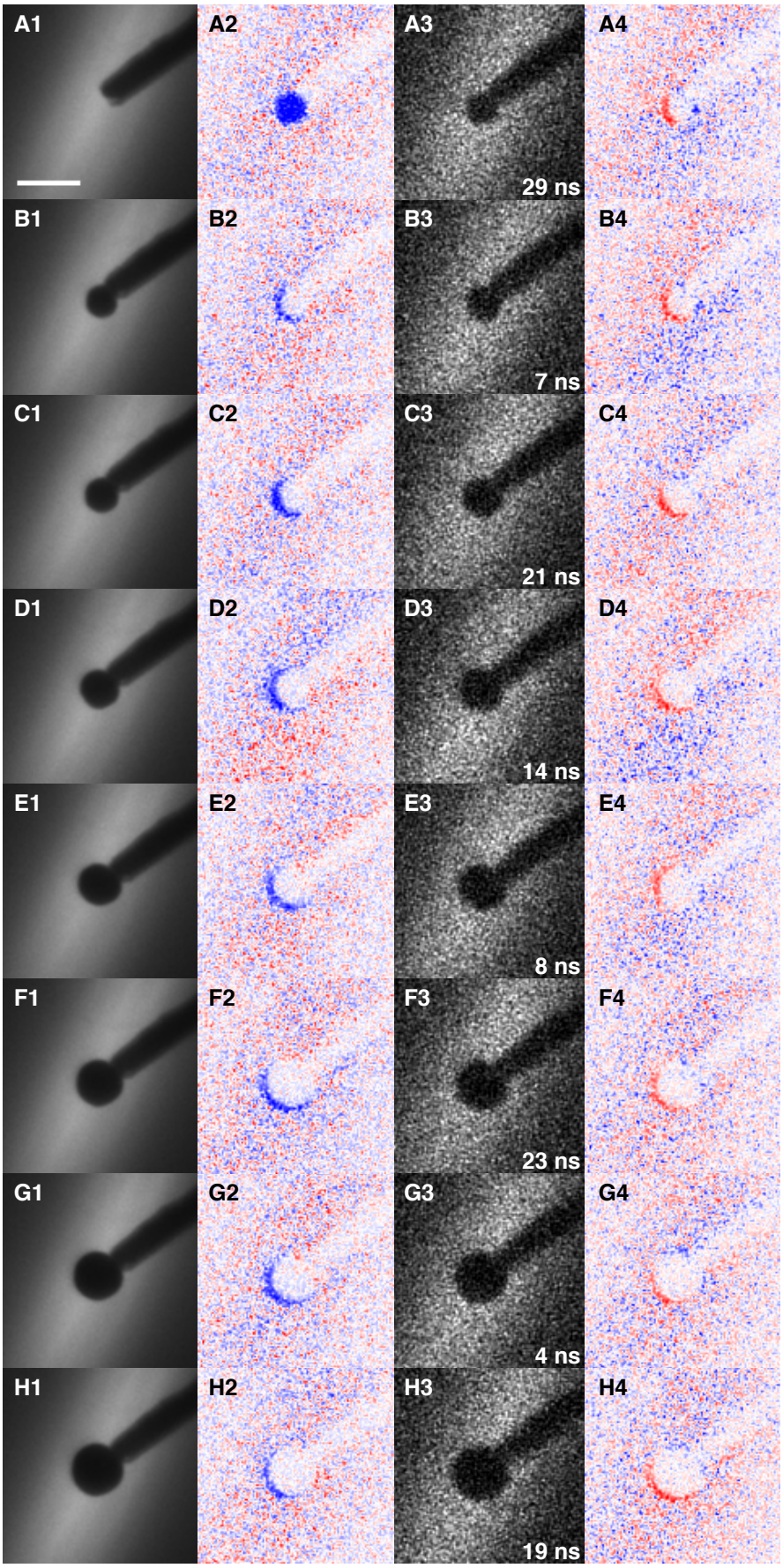
A1
A2
A3
29 ns
A4
B1
B2
B3
7 ns
B4
C1
C2
C3
21 ns
C4
D1
D2
D3
14 ns
D4
E1
E2
E3
8 ns
E4
F1
F2
F3
23 ns
F4
G1
G2
G3
4 ns
G4
H1
H2
H3
19 ns
H4

Fig. S5. Lead leaking from the open end of a ZnO nanotube in a series of single-shot experiments. **(A1, B1, ...)** Images of the nanotube before each pump laser pulse, acquired by accumulating over 600 electron pulses. **(A3, B3, ...)** Single-shot images taken at short delays after the heating pulse. **(A2, B2, ...)** Difference images obtained by subtracting the images recorded before each pump laser pulse from the single-shot images. Negative and positive intensity are indicated by blue and red, respectively. **(A4, B4, ...)** Difference images obtained by subtracting the single-shot images from the images recorded after each pump pulse. (Scale bar, 200 nm.)

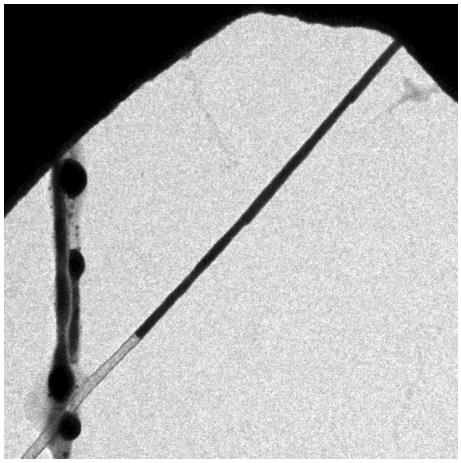

Fig. S6. Micrograph of the nanotube in Fig. 4 of the main text. On the left, two other tubes were damaged during laser irradiation. The copper mesh of the TEM grid is visible at the top. (Scale bar, 300 nm)

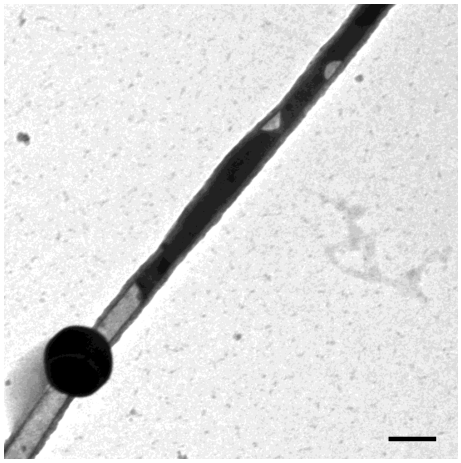

Movie S1. Movie of a lead filled ZnO nanotube during irradiation with a picosecond pulsed laser. Images were recorded every 4 s with a continuous electron beam and 1 s acquisition time, while the nanotube was irradiated at 0.5 Hz repetition rate with a pulse energy of 150 nJ. In order to correct for any drift, the images were aligned using cross correlation with a reference. (Scale bar, 100 nm.)

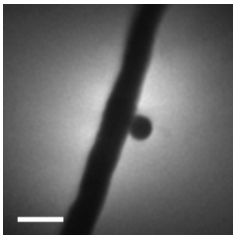

Movie S2. Movie of a lead filled ZnO nanotube reabsorbing a spherical extrusion. The extrusion had been created by a single laser pulse, which had forced part of the molten core through a leak in the tube wall. Images were recorded every 5 s with a pulsed electron beam (2 kHz repetition rate) and 0.3 s acquisition time. The sample was held at 363 K and was not irradiated with the pump laser while the movie was recorded. (Scale bar, 200 nm.)

References and Notes

1. J. C. T. Eijkel, A. van den Berg, Nanofluidics: What is it and what can we expect from it? *Microfluid. Nanofluid.* **1**, 249–267 (2005). doi:10.1007/s10404-004-0012-9

2. L. Bocquet, E. Charlaix, Nanofluidics, from bulk to interfaces. *Chem. Soc. Rev.* **39**, 1073–1095 (2010). Medline doi:10.1039/b909366b

3. M. Majumder, N. Chopra, R. Andrews, B. J. Hinds, Nanoscale hydrodynamics: Enhanced flow in carbon nanotubes. *Nature* **438**, 44 (2005). Medline doi:10.1038/438044a

4. J. K. Holt, H. G. Park, Y. Wang, M. Stadermann, A. B. Artyukhin, C. P. Grigoropoulos, A. Noy, O. Bakajin, Fast mass transport through sub-2-nanometer carbon nanotubes. *Science* **312**, 1034–1037 (2006). Medline doi:10.1126/science.1126298

5. M. Whitby, L. Cagnon, M. Thanou, N. Quirke, Enhanced fluid flow through nanoscale carbon pipes. *Nano Lett.* **8**, 2632–2637 (2008). Medline doi:10.1021/nl080705f

6. M. Whitby, N. Quirke, in *Handbook of Nanophysics: Nanotubes and Nanowires*, K. D. Sattler, Ed. (CRC Press, Boca Raton, FL, 2011), chap. 11.

7. J. M. Yuk, J. Park, P. Ercius, K. Kim, D. J. Hellebusch, M. F. Crommie, J. Y. Lee, A. Zettl, A. P. Alivisatos, High-resolution EM of colloidal nanocrystal growth using graphene liquid cells. *Science* **336**, 61–64 (2012). Medline doi:10.1126/science.1217654

8. Q. Chen, J. M. Smith, J. Park, K. Kim, D. Ho, H. I. Rasool, A. Zettl, A. P. Alivisatos, 3D motion of DNA-Au nanoconjugates in graphene liquid cell electron microscopy. *Nano Lett.* **13**, 4556–4561 (2013). Medline doi:10.1021/nl402694n

9. N. Naguib, H. H. Ye, Y. Gogotsi, A. G. Yazicioglu, C. M. Megaridis, M. Yoshimura, Observation of water confined in nanometer channels of closed carbon nanotubes. *Nano Lett.* **4**, 2237–2243 (2004). doi:10.1021/nl0484907

10. J. Y. Chen, A. Kutana, C. P. Collier, K. P. Giapis, Electrowetting in carbon nanotubes. *Science* **310**, 1480–1483 (2005). Medline doi:10.1126/science.1120385

11. Y. Gogotsi, J. A. Libera, A. Guvenc-Yazicioglu, C. M. Megaridis, In situ multiphase fluid experiments in hydrothermal carbon nanotubes. *Appl. Phys. Lett.* **79**, 1021–1023 (2001). doi:10.1063/1.1391228

12. M. P. Rossi, H. H. Ye, Y. Gogotsi, S. Babu, P. Ndungu, J. C. Bradley, Environmental scanning electron microscopy study of water in carbon nanopipes. *Nano Lett.* **4**, 989–993 (2004). doi:10.1021/nl049688u

13. A. Siria, P. Poncharal, A. L. Biance, R. Fulcrand, X. Blase, S. T. Purcell, L. Bocquet, Giant osmotic energy conversion measured in a single transmembrane boron nitride nanotube. *Nature* **494**, 455–458 (2013). Medline doi:10.1038/nature11876

14. A. H. Zewail, Four-dimensional electron microscopy. *Science* **328**, 187–193 (2010). Medline doi:10.1126/science.1166135

15. A. H. Zewail, J. M. Thomas, *4D Electron Microscopy: Imaging in Space and Time* (Imperial College Press, London, 2010).

16. See supplementary materials on *Science* Online.

17. C.-Y. Wang, N.-W. Gong, L.-J. Chen, High-sensitivity solid-state Pb(core)/ZnO(shell) nanothermometers fabricated by a facile galvanic displacement method. *Adv. Mater.* **20**, 4789–4792 (2008). doi:10.1002/adma.200703233

18. P. J. Linstrom, W. G. Mallard, Eds., *Thermodynamics Source Database* (NIST Chemistry WebBook, NIST Standard Reference Database No. 69; National Institute of Standards and Technology, Gaithersburg, MD, 2014).

19. S. Link, C. Burda, B. Nikoobakht, M. A. El-Sayed, How long does it take to melt a gold nanorod? A femtosecond pump-probe absorption spectroscopic study. *Chem. Phys. Lett.* **315**, 12–18 (1999). doi:10.1016/S0009-2614(99)01214-2

20. C. Y. Ruan, Y. Murooka, R. K. Raman, R. A. Murdick, Dynamics of size-selected gold nanoparticles studied by ultrafast electron nanocrystallography. *Nano Lett.* **7**, 1290–1296 (2007). Medline doi:10.1021/nl070269h

21. H. Sakai, Surface-induced melting of small particles. *Surf. Sci.* **351**, 285–291 (1996). doi:10.1016/0039-6028(95)01263-X

22. P.-G. de Gennes, F. Brochard-Wyart, D. Quere, *Capillarity and Wetting Phenomena: Drops, Bubbles, Pearls, Waves* (Springer, New York, 2004).

23. Similar values for f were obtained when x_e was varied. We determined f_0 to be 2.14×10^{-2} Pa·s using the viscosity of bulk lead at 1700 K, the estimated temperature of the tube after the laser pulse (*16*); shear thinning is expected to be insignificant despite the high shear rate in our experiment (*32*). For other nanotubes of larger diameter, on the order of 100 nm, similar friction coefficients were obtained.

24. M. Whitby, N. Quirke, Fluid flow in carbon nanotubes and nanopipes. *Nat. Nanotechnol.* **2**, 87–94 (2007). Medline doi:10.1038/nnano.2006.175

25. L. Bocquet, J. L. Barrat, Flow boundary conditions from nano- to micro-scales. *Soft Matter* **3**, 685–693 (2007). doi:10.1039/b616490k

26. D. Chatain, Anisotropy of wetting. *Annu. Rev. Mater. Res.* **38**, 45–70 (2008). doi:10.1146/annurev.matsci.38.060407.130210

27. Q. Xu, N. Oudalov, Q. T. Guo, H. M. Jaeger, E. Brown, Effect of oxidation on the mechanical properties of liquid gallium and eutectic gallium-indium. *Phys. Fluids* **24**, 063101 (2012). doi:10.1063/1.4724313

28. G. Yi, W. Schwarzacher, Single crystal superconductor nanowires by electrodeposition. *Appl. Phys. Lett.* **74**, 1746–1748 (1999). doi:10.1063/1.123675

29. P. A. Thompson, S. M. Troian, A general boundary condition for liquid flow at solid surfaces. *Nature* **389**, 360–362 (1997). doi:10.1038/38686

30. C. Cottin-Bizonne, B. Cross, A. Steinberger, E. Charlaix, Boundary slip on smooth hydrophobic surfaces: Intrinsic effects and possible artifacts. *Phys. Rev. Lett.* **94**, 056102 (2005). Medline doi:10.1103/PhysRevLett.94.056102

31. E. Tajkhorshid, P. Nollert, M. O. Jensen, L. J. W. Miercke, J. O'Connell, R. M. Stroud, K. Schulten, Control of the selectivity of the aquaporin water channel family by global orientational tuning. *Science* **296**, 525–530 (2002). doi:10.1126/science.1067778

32. C. Desgranges, J. Delhommelle, Rheology of liquid fcc metals: Equilibrium and transient-time correlation-function nonequilibrium molecular dynamics simulations. *Phys. Rev. B* **78**, 184202 (2008). doi:10.1103/PhysRevB.78.184202

33. *Handbook on Lead-Bismuth Eutectic Alloy and Lead Properties, Materials Compatibility, Thermal-Hydraulics and Technologies* (Nuclear Energy Agency, Organisation for Economic Co-operation and Development, 2007).

34. J. W. Herman, H. E. Elsayed-Ali, Superheating of Pb(111). *Phys. Rev. Lett.* **69**, 1228–1231 (1992). Medline doi:10.1103/PhysRevLett.69.1228

35. A. Plech, V. Kotaidis, S. Gresillon, C. Dahmen, G. von Plessen, Laser-induced heating and melting of gold nanoparticles studied by time-resolved x-ray scattering. *Phys. Rev. B* **70**, 195423 (2004). doi:10.1103/PhysRevB.70.195423

36. M. W. Chase, NIST-JANAF Thermochemical Tables (National Institute of Standards and Technology, Woodbury, NY, ed. 4, 1998).

37. R. Pässler, Characteristic non-Debye heat capacity formula applied to GaN and ZnO. *J. Appl. Phys.* **110**, 043530 (2011). doi:10.1063/1.3622668

38. M. Bauer, M. Aeschlimann, Dynamics of excited electrons in metals, thin films and nanostructures. *J. Electron Spectrosc. Relat. Phenom.* **124**, 225–243 (2002). doi:10.1016/S0368-2048(02)00056-7

39. S. Stølen, F. Gronvold, Critical assessment of the enthalpy of fusion of metals used as enthalpy standards at moderate to high temperatures. *Thermochim. Acta* **327**, 1–32 (1999). doi:10.1016/S0040-6031(98)00613-3

40. S. Timoshenko, *Vibration Problems in Engineering* (Van Nostrand, New York, ed. 2, 1937).